Supporting Information

Heterostructure engineering enables $MoSe_2$ with superior Li/Na-ion storage

Huabin Kong,[#] Yihan Wen, Siyin Chen, Xiyao Chen, Runzhi Chen, Jiamou Yan, Nianjie Mao*

Department of Materials Science and Engineering, Huaqiao University, Xiamen, 361021, China

# These authors contributed equally to this work

Corresponding Authors

* Huabin Kong, E-mail: konghuabin@hqu.edu.cn

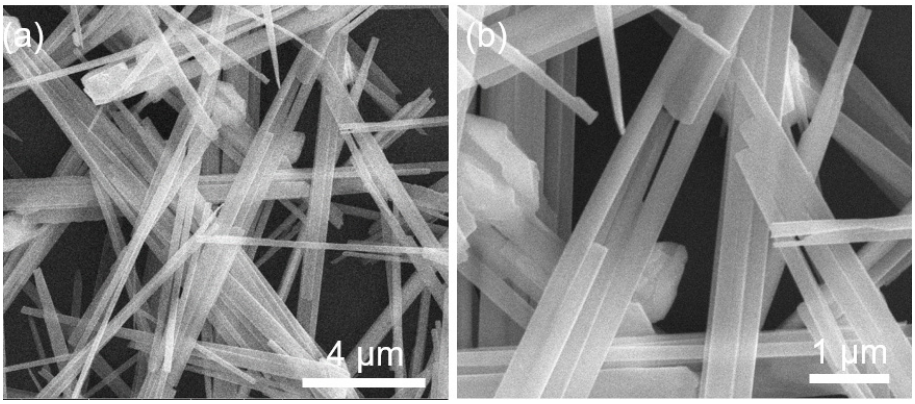

Figure S1. The SEM images of $MoSe_2$.

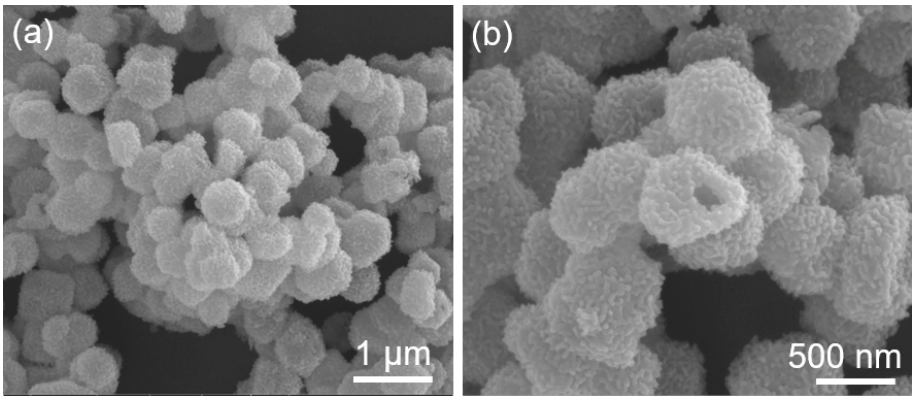

Figure S2. The SEM images of $CoSe_2$/NC.

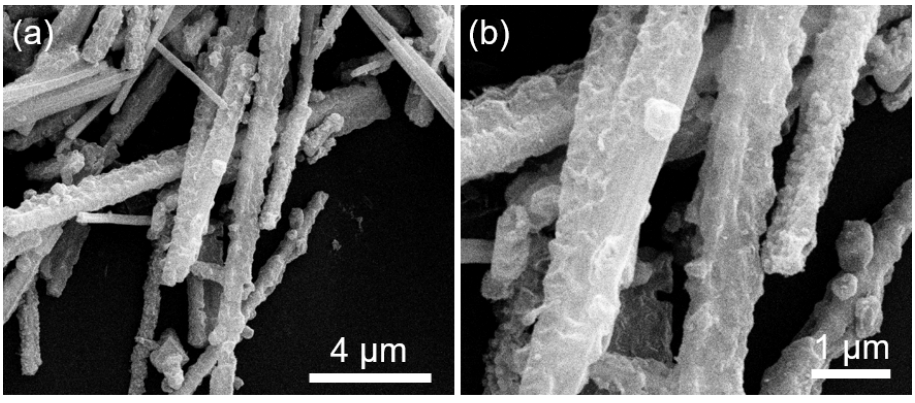

Figure S3. The SEM images of $MoSe_2$/$CoSe_2$/NC.

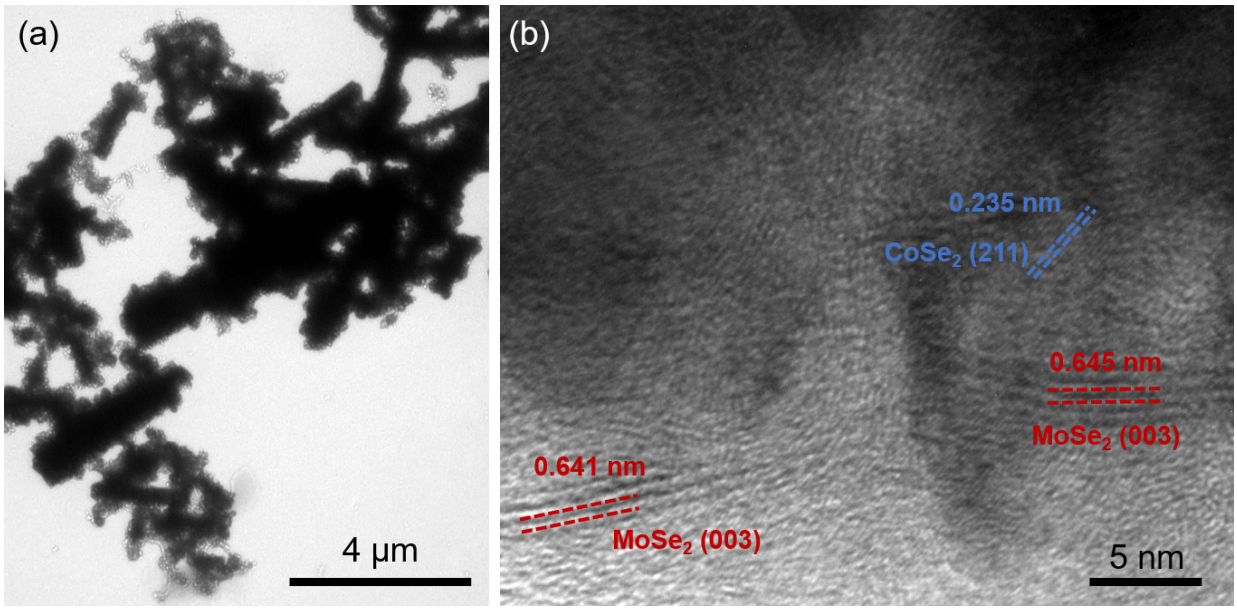

Figure S4. The TEM and HRTEM images of $MoSe_2/CoSe_2/NCNFs$.

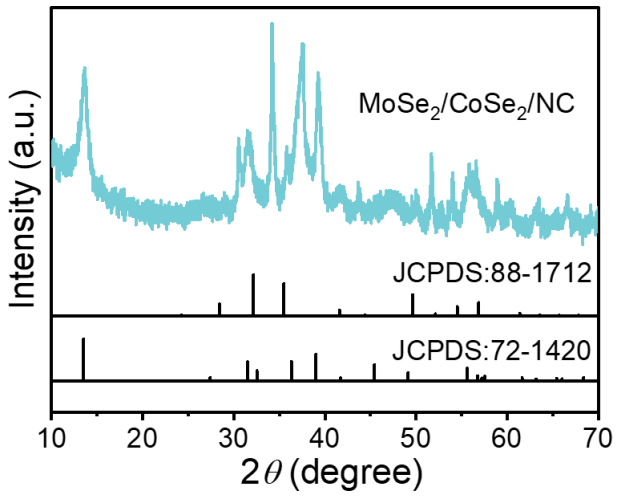

Figure S5. The XRD pattern of $MoSe_2/CoSe_2/NC$.

Calculation process of each substance content in the $MoSe_2/CoSe_2$/NCNTs

In the thermogravimetric measurement, the chemical reactions occurred as follows:

$3CoSe_2 + 8O_2 \longrightarrow Co_3O_4 + 6SeO_2$ $MoSe_2 + 3.5O_2 \longrightarrow MoO_3 + SeO_2$

$SeO_2 \longrightarrow Se\uparrow + O_2\uparrow$ $C + O_2 \longrightarrow CO_2\uparrow$

Therefore, the final product after testing (29.77%) is Co_3O_4 and MoO_3. The increase of mass (25.38%) during measurement is mainly due to the inclusion of oxygen atoms. And the loss of mass (93.23%) during measurement is mainly due to the disappearance of carbon and SeO_2.

Set the mole number of Co_3O_4 as a and the mole number of MoO_3 as b. Therefore, the following two equations can be listed:

$$241a + 144b = 36.1\ \% \qquad 256a + 112b = 32.0\%$$

$$a = 0.058\% \qquad b = 0.155\%$$

The mass percent of $CoSe_2 = 217 \times 3 \times 0.058\% = 38\%$

The mass percent of $MoSe_2 = 254 \times 0.155\% = 40\%$

The mass percent of NC = 100% – 38% – 40% = 22 %

So the contents of $MoSe_2$, $CoSe_2$ and NCNTs are 40%, 38% and 22% in the $MoSe_2/CoSe_2$/NCNTs, respectively.

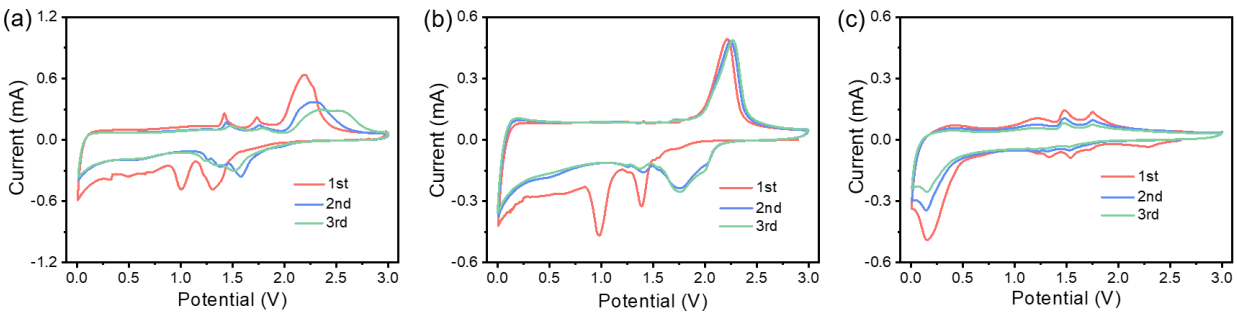

Figure S6. The CV curves of samples at a scan rate of 0.5 mV s^{-1} in LIBs: (a) $MoSe_2/CoSe_2/NC$, (b) $CoSe_2/NC$, (c) $MoSe_2$.

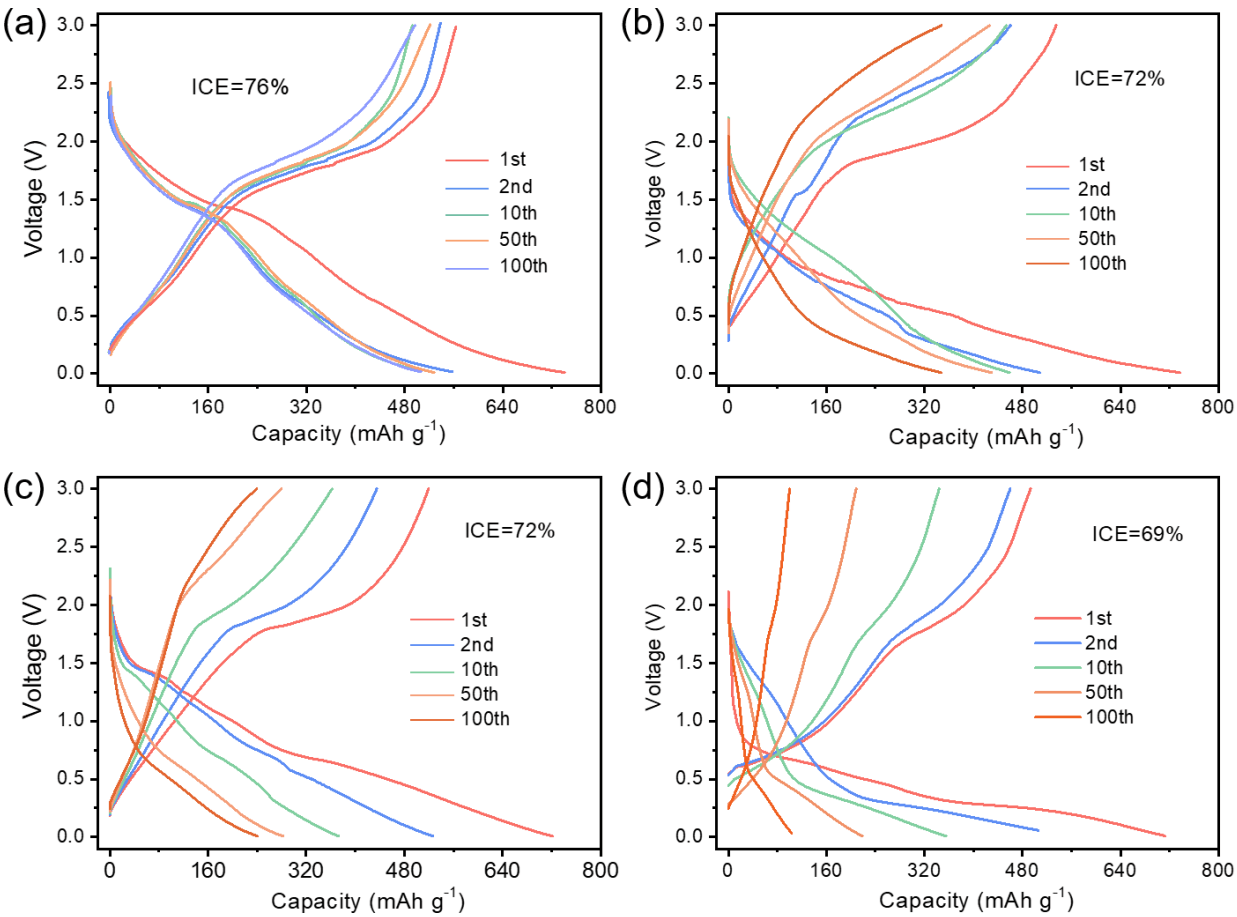

Figure S7. The charge/discharge profiles of samples at a current density of 0.2 A g^{-1} in LIBs: (a) $MoSe_2/CoSe_2/NCNFs$, (b) $MoSe_2/CoSe_2/NC$, (c) $CoSe_2/NC$, (d) $MoSe_2$.

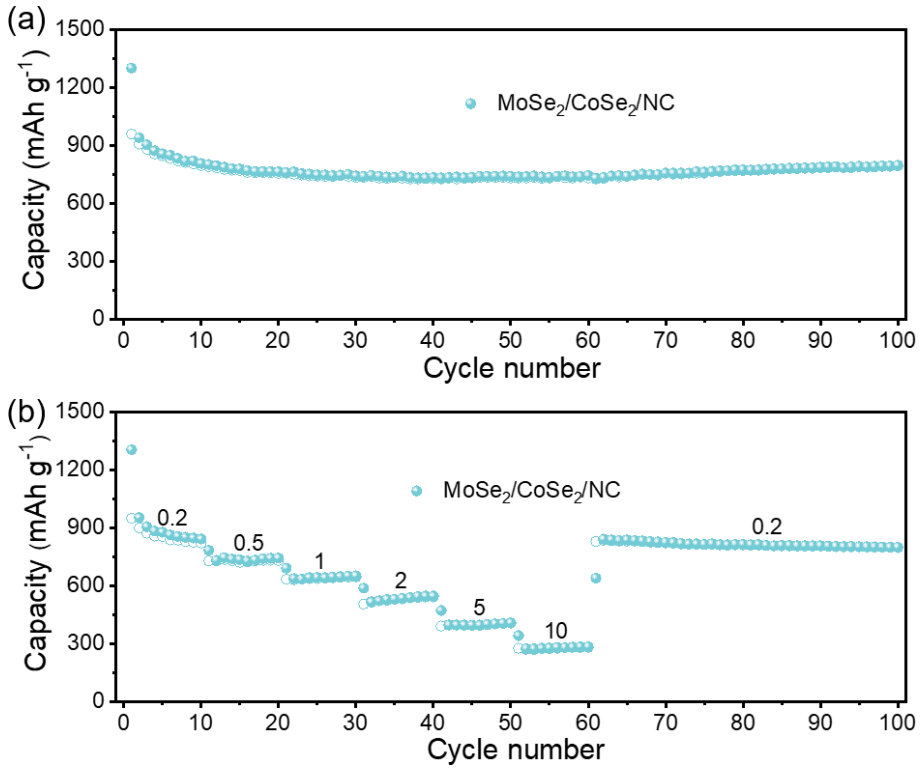

Figure S8. Electrochemical performances of $MoSe_2/CoSe_2$/NC in LIBs: (a) Cycling performances at 0.2A g^{-1}, (b) Rate performances at 0.2-10 A g^{-1}.

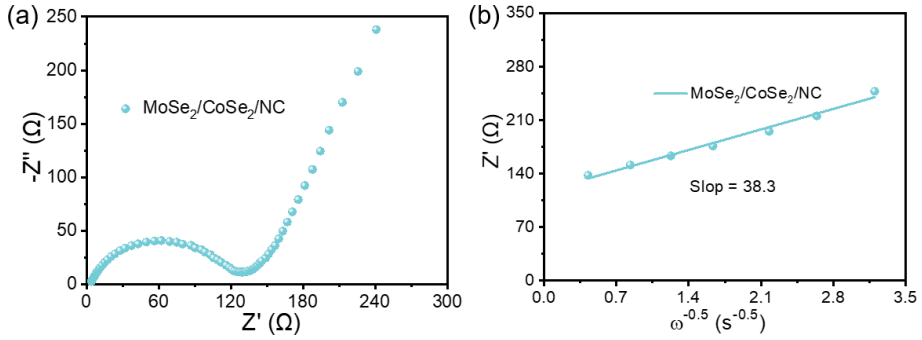

Figure S9. (a) Nyquist plots of $MoSe_2/CoSe_2$/NC after 100 cycles in LIBs and (b) The relationship between Z_{re} and $\omega^{-1/2}$.

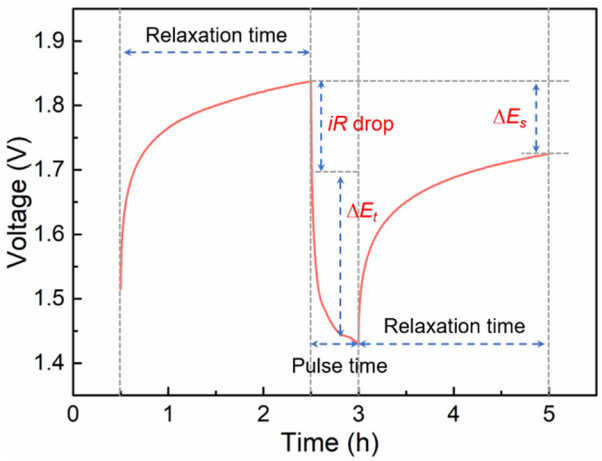

Figure S10. E vs. t curves of the $MoSe_2/CoSe_2$/NC for a single GITT during discharge process.

The lithium diffusion coefficient was measured by using Galvanostatic intermittent titration technique (GITT) and calculated based on equation as follows.

$$D = \frac{4L^2}{\pi\tau}\left(\frac{\Delta E_s}{\Delta E_t}\right)^2$$

Where L is lithium ion diffusion length (unit : cm); for compact electrode, it is equal to average thickness of pole piece measured, τ is the relaxation tim e (unit : s), and ΔE_s is the steady-state potential (unit : V) by the current pluse. ΔE_t is the potential change (unit : V) during the constant current pluse after eliminating the iR drop.

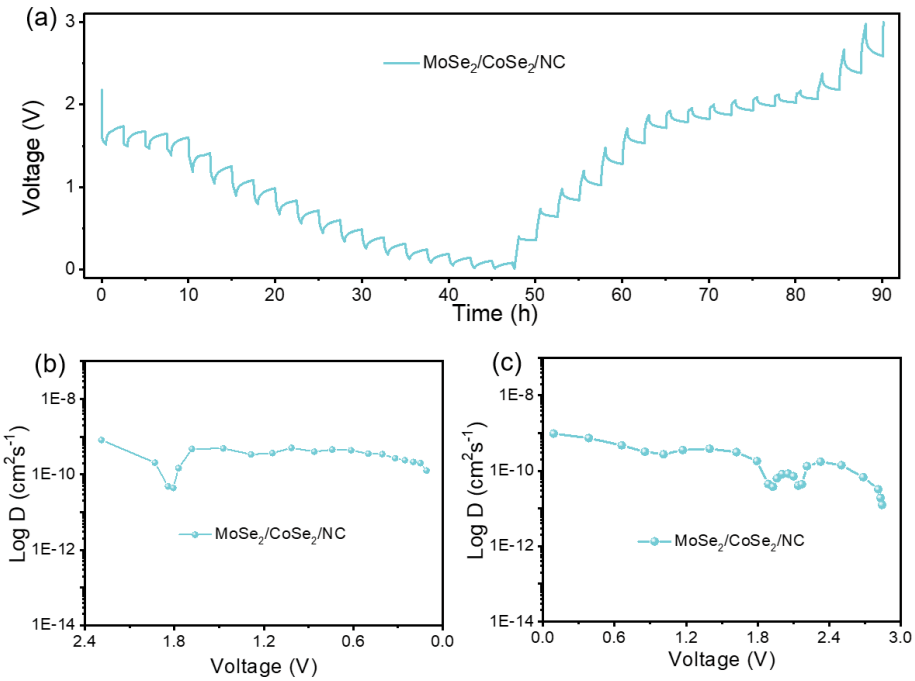

Figure S11. Electrochemical performances of $MoSe_2/CoSe_2/NC$ in LIBs: (a) GITT curves at 5th discharge and charge process, (b, c) the corresponding Li^+ diffusion coefficient at 5th discharge and charge process.

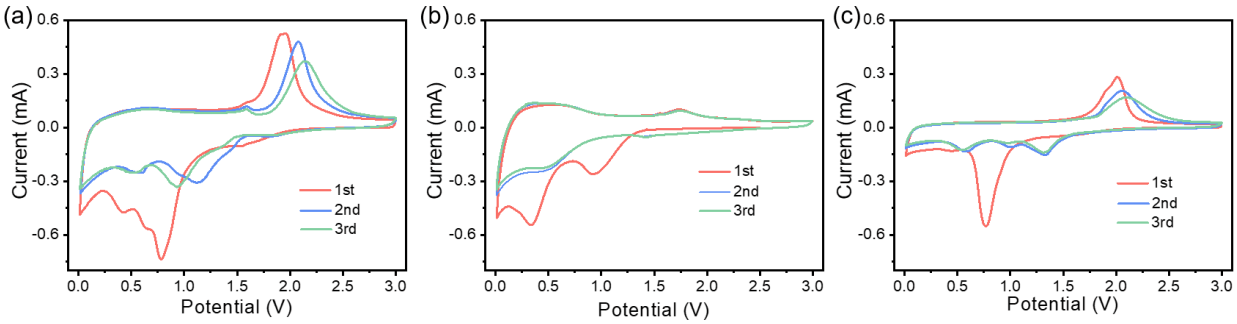

Figure S12. The CV curves of samples at a scan rate of 0.5 mV s^{-1} in SIBs: (a) $MoSe_2/CoSe_2/NC$, (b) $CoSe_2/NC$, (c) $MoSe_2$.

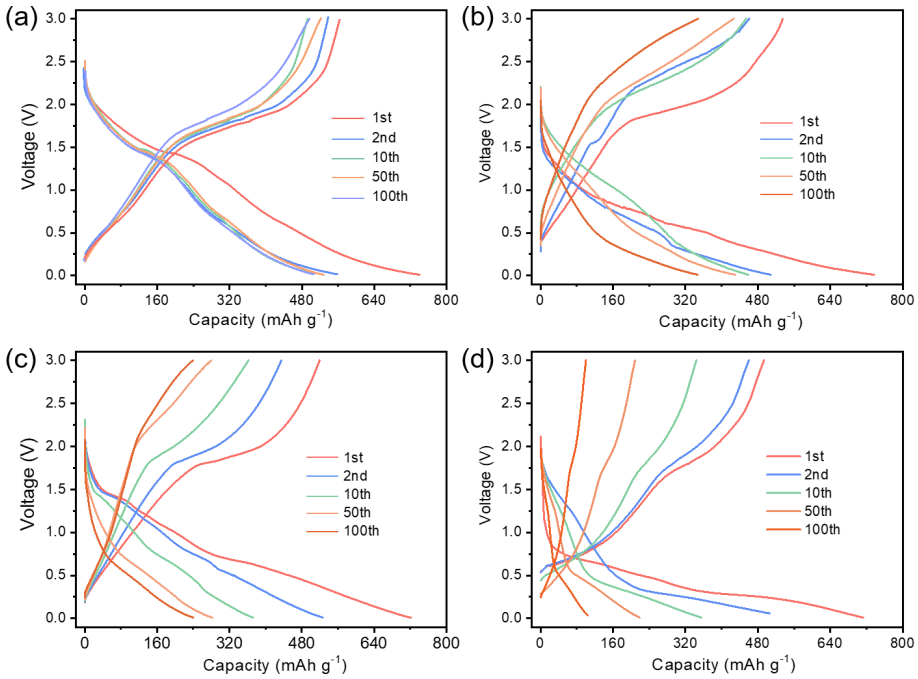

Figure S13. The charge/discharge profiles of samples at a current density of 0.2 A g^{-1} in SIBs: (a) $MoSe_2/CoSe_2$/NCNFs, (b) $MoSe_2/CoSe_2$/NC, (c) $CoSe_2$/NC, (d) $MoSe_2$

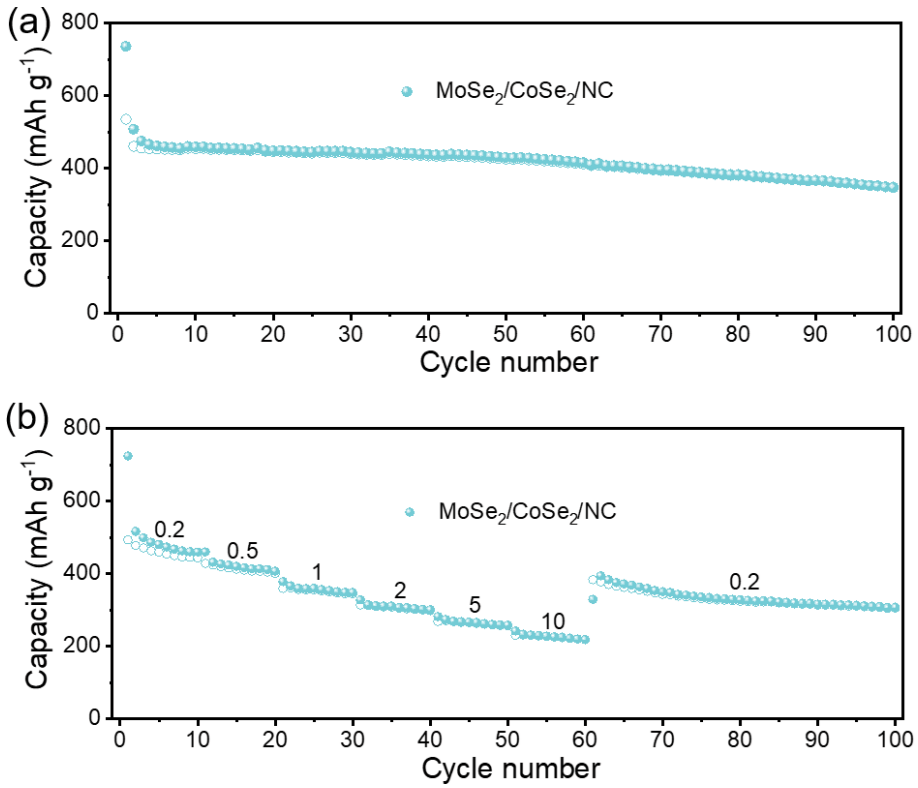

Figure S14. Electrochemical performances of $MoSe_2/CoSe_2$/NC in SIBs: (a) Cycling performances at 0.2A g^{-1}, (b) Rate performances at 0.2-10 A g^{-1}.

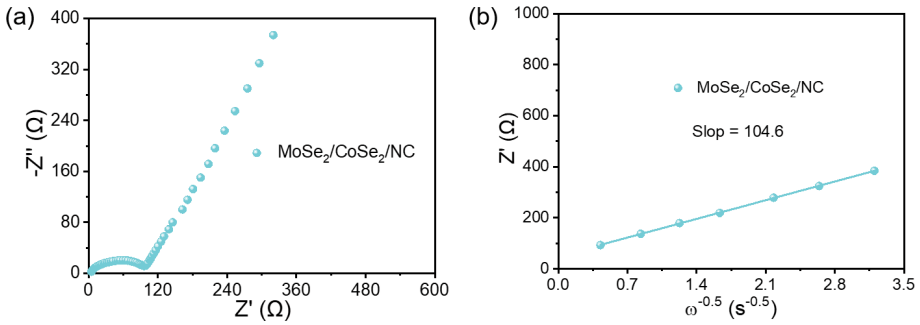

Figure S15. (a) Nyquist plots of $MoSe_2/CoSe_2/NC$ after 100 cycles in SIBs and (b) The relationship between Z_{re} and $\omega^{-1/2}$.

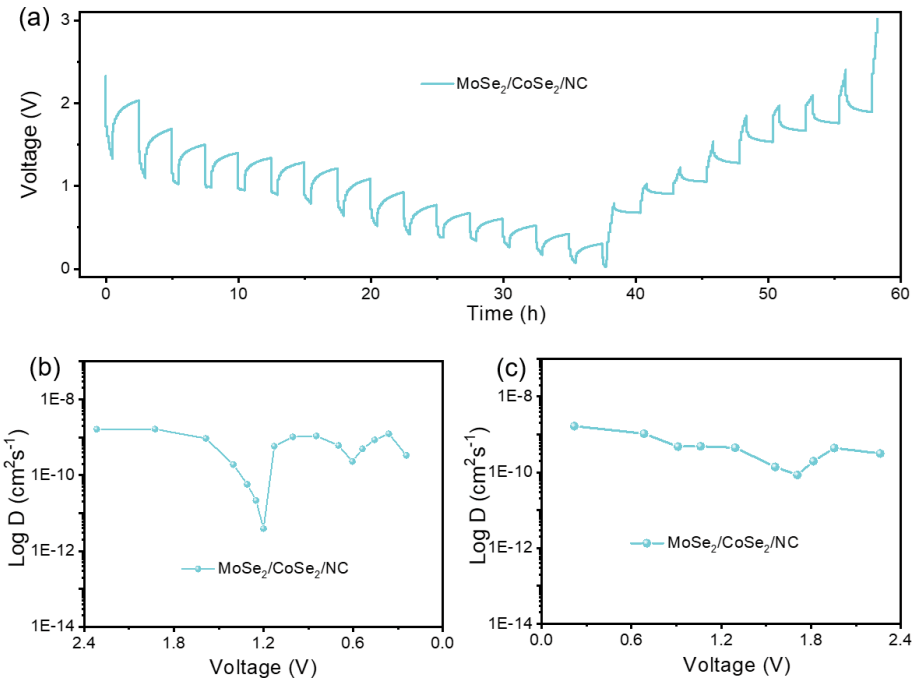

Figure S16. Electrochemical performances of $MoSe_2/CoSe_2/NC$ in SIBs: (a) GITT curves at 5th discharge and charge process, (b, c) the corresponding Li^+ diffusion coefficient at 5th discharge and charge process.

Table S1. Comparison of electrochemical performance in LIBs between $MoSe_2/CoSe_2$/NC and previously reported literature.

LIB anode material	Rate performance ($mAh\ g^{-1}$)	Cycling performance ($mAh\ g^{-1}$)	Published year
This work	**452 at 10 A g^{-1}**	**553 after 2000 cycles at 5 A g^{-1}**	
$MoSe_2$@NC SNCs[1]	124 at 16 A g^{-1}	501 after 320 cycles at 2 A g^{-1}	2021
$MoSe_2$@N-C[2]	300 at 10 A g^{-1}	360 after 500 cycles at 5 A g^{-1}	2020
$MoSe_2$ nanoparticles[3]	423 at 5 A g^{-1}	573 after 200 cycles at 0.2 A g^{-1}	2022
Mo-$MoSe_2$[4]	380 at 10 C	550 after 50 cycles at 0.2 C	2020
NHMCFs/$MoSe_2$[5]	244 at 10 A g^{-1}	582 after 400 cycles at 1 A g^{-1}	2021
MoO_2@$MoSe_2$@NC[6]	311 at 5 A g^{-1}	468 after 80 cycles at 0.5 A g^{-1}	2021
$MoSe_2$/MoC/N–C[7]	575 at 4 A g^{-1}	535 after 5000 cycles at 2 A g^{-1}	2020
$MoSe_2$@NCNFs[8]	250 at 2 A g^{-1}	180 after 500 cycles at 2 A g^{-1}	2024
Ag/$MoSe_2$[9]	325 at 2 A g^{-1}	497 after 500 cycles at 0.5 A g^{-1}	2021
$MoSe_2$/NFC[10]	298 at 5 A g^{-1}	306 after 500 cycles at 2 A g^{-1}	2020
MWSe[11]	438 at 5 A g^{-1}	1007 after 500 cycles at 0.5 A g^{-1}	2023
$MoSe_2$@rGO&CNT[12]	126 at 1.2 A g^{-1}	376 after 50 cycles at 0.06 A g^{-1}	2022

Table S2. Comparison of electrochemical performance in SIBs between $MoSe_2/CoSe_2$/NC and previously reported literature.

SIB anode material	Rate performance ($mAh\ g^{-1}$)	Cycling performance ($mAh\ g^{-1}$)	Published year
This work	**296 at 10 A g^{-1}**	**310 after 2000 cycles at 5 A g^{-1}**	
$MoSe_2/SnSe_2$@C[13]	350 at 1.6 A g^{-1}	324 after 200 cycles at 0.5 A g^{-1}	2023
$MoSe_2$/N-PCD[14]	266 at 2 A g^{-1}	270 after 1000 cycles at 2 A g^{-1}	2020
$MoSe_2$ nanoplatelets[15]	196 at 10 A g^{-1}	270 after 2500 cycles at 2 A g^{-1}	2020
$MoSe_2$/MXene[16]	250 at 10 A g^{-1}	380 after 400 cycles at 2 A g^{-1}	2020
$MoSe_2$@rGO[17]	251 at 5 A g^{-1}	225 after 100 cycles at 0.5 A g^{-1}	2021
$CoSe_2$–$MoSe_2$/rGO[18]	393 at 5 A g^{-1}	326 after 500 cycles at 2 A g^{-1}	2022
P-1T-$MoSe_2$[19]	275 at 10 A g^{-1}	328 after 1000 cycles at 5 A g^{-1}	2022
P-$MoSe_2$/N-CNT[22]	169 at 10 A g^{-1}	372 after 300 cycles at 0.2 A g^{-1}	2021
NC@$MoSe_2$@rGO[21]	200 at 2 A g^{-1}	186 after 100 cycles at 1 A g^{-1}	2021
PEG-C@$MoSe_2$@CNT[22]	392 at 3 A g^{-1}	212 after 3000 cycles at 2 A g^{-1}	2023
C@$MoSe_2$@NMWCNT[23]	126 at 10 A g^{-1}	168 after 3600 cycles at 2 A g^{-1}	2023
$MoSe_2$⊂CNB[24]	124 at 10 A g^{-1}	140 after 7500 cycles at 10 A g^{-1}	2021

Reference

[1] Liu, Y; Cao, J; Cai, J; Chen, M; Wang, L; Huang, X; Liao, S; Min, Y. Flower-like $MoSe_2$@N-doped carbon sub-nanoclusters regulated by MoO_3 hexagonal prism as advanced anode for lithium-ion battery. *J. Alloys Compd.* **2021**, 865, 158276.

[2] Zhang, K; Jiang, X; Zeng, M; Jing, B. Hydrothermal synthesis of three-dimensional hydrangea-like $MoSe_2$@N-doped carbon anode material for high performance lithium ion batteries. *J. Electroanal. Chem.* **2020**, 879, 114818.

[3] Li, N; Zhou, Q; Lin, J; Lu, Y; Hou, Z; Qian, Y. One-pot synthesis of uniform $MoSe_2$ nanoparticles as high performance anode materials for lithium/sodium ion batteries. *J. Alloy Compd.* **2022**, 922, 166306.

[4] Wu, Y; Liu, W. Few-layered $MoSe_2$ ultrathin nanosheets as anode materials for lithium ion batteries. *J. Alloys Compd.* **2020**, 813, 152074.

[5] Ni, X; Cui, Z; Luo, H; Chen, H; Liu, C; Wu, Q; Ju, A. Hollow multi-nanochannel carbon nanofibers@$MoSe_2$ nanosheets composite as flexible anodes for high performance lithium-ion batteries. *Chem. Eng. J.* **2021**, 404, 126249.

[6] Qin, Z; Liu, X; Huang, Z; Sun, R; Li, Z; Fan, H; Lu, S. Electrochemical and pseudocapacitive analysis of rod-like MoO_2@$MoSe_2$@NC heterostructures for high-performance lithium ion batteries. *Acta Metall. Sin. (Engl. Lett.)* **2021**, 34, 425–434.

[7] Chen, J; Luo, Y; Zhang, W; Qiao, Y; Cao, X; Xie, X; Zhou, H; Pan, A; Liang, S. Tuning interface bridging between $MoSe_2$ and three-dimensional carbon framework by incorporation of MoC intermediate to boost lithium storage capability. *Nano-Micro Lett.* **2020**, 12, 171.

[8] Cu, Q; Shang, C; Zhou, G; Wang, X. Freestanding $MoSe_2$ nanoflowers for superior Li/Na storage properties. *Tungsten.* **2024**, 6, 238-247.

[9] Ni, X.; Cui, Z.; Luo, H.; Chen, H.; Liu, C.; Wu, Q.; Ju, A. Hollow multi-nanochannel carbon nanofibers@$MoSe_2$ nanosheets composite as flexible anodes for high performance lithium-ion batteries. *Chem. Eng. J.* **2021**, 404, 126249.

[10] Wang, S.; Si, Y.; Wan, P.; Zhu, S.; Chu, W.; Yu, Z. $MoSe_2$ nanoflowers grown on 3D carbon network as an advanced anode for lithium ion batteries. *Mater. Lett.* **2022**, 310, 131487.

[11] Wang, K.; Zhou, Y.; Cheng, L.; Li, D.; Hu, Z.; Chen, S.; Wu, C.; Song, L.; Ge, B. Engineering phase transition from 2H to 1T in $MoSe_2$ by W cluster doping toward lithium-ion battery. *Inorg. Chem.* **2023**, 62, 21257-21264.

[12] Li, J.; Sun, L.; Li, H.; Zhang, Y.; Yang, Y.; Luo, Y.; Qin, Y.; Wang, J. $MoSe_2$ nanosheets anchored on carbon nanofibers as advanced anodes for lithium-ion batteries. *Electrochim. Acta.* **2023**, 426, 140743.

[13] Wang, W.; Hu, L.; Li, L.; Liu, C.; Liu, X.; Wang, H.; Zhai, G. Constructing a rapid ion and electron migration channels in $MoSe_2$/$SnSe_2$@C 2D heterostructures for high-efficiency sodium-ion half/full batteries. *Electrochim. Acta* **2023**, 449, 142239.

[14] Xie, X.; Huang, K.; Wu, X.; Wu, N.; Xu, Y.; Zhang, S.; Zhang, C. Binding hierarchical $MoSe_2$ on MOF-derived N-doped carbon dodecahedron for fast and durable sodium-ion storage. *Carbon* **2020**, 169, 1-8.

[15] Zhao, X.; Zhao, Y.; Huang, B.; Cai, W.; Sui, J.; Yang, Z.; Wang, H.-E. $MoSe_2$ nanoplatelets with enriched active edge sites for superior sodium-ion storage and enhanced alkaline hydrogen evolution activity. *Chem. Eng. J.* **2020**, 382, 123047.

[16] Xu, E.; Zhang, Y.; Wang, H.; Zhu, Z.; Quan, J.; Chang, Y.; Li, P.; Yu, D.; Jiang, Y. Ultrafast kinetics net electrode assembled via $MoSe_2$/MXene heterojunction for high-performance sodium-ion batteries. *Chem. Eng. J.* **2019**, 382, 123839.

[17] Chong, S.; Wei, X.; Wu, Y.; Sun, L.; Shu, C.; Lu, Q.; Hu, Y.; Cao, G.; Huang, W. Expanded $MoSe_2$ nanosheets vertically bonded on reduced graphene oxide for sodium and potassium-ion storage. *ACS Appl. Mater. Interfaces* **2021**, 13, 13158-13169.

[18] Xu, Y; Liu, X; Su, H; Jiang, S; Zhang, J; Li, D. Hierarchical bimetallic selenides $CoSe_2$–$MoSe_2$/rGO for sodium/potassium-ion batteries anode: insights into the intercalation and conversion mechanism. *Energy Environ. Mater.* **2022**, 5, 627–636.

[19] He, H; Zhang, H; Huang, D; Kuang, W; Li, X; Hao, J; Guo, Z; Zhang, C. Harnessing plasma-assisted doping engineering to stabilize metallic phase $MoSe_2$ for fast and durable sodium-ion storage. *Adv. Mater.* **2022**, 34, 2200397.

[20] Seon, Y; Kang, Y; Cho, J. One-dimensional porous nanostructure composed of few-layered $MoSe_2$ nanosheets and highly densified-entangled-N-doped CNTs as anodes for Na ion batteries. *Chem. Eng. J.* **2021**, 425, 129051.

[21] Yang, Y; Wang, F; Chen, Y; Chen, C; Zhang, S; Yu, Z; Au, C; Yin, S; Qiu, R. Building a PEG-C@$MoSe_2$@CNT heterostructure via in-situ selenidation as highly reversible anodes for Na^+ batteries. *Sci. China Chem.* **2023**, 66, 475–491.

[22] Chen, S; Shi, Y; Ma, L; Li, N; Wang, Z; Wu, M. Selenide-based anodes for advanced sodium-ion batteries. *Energy Environ. Sci.* **2023**, 16, 1074–1096.

[23] Yang, Y; Wang, F; Bian, M; Chen, Y; Zhang, S; Yu, Z; Au, C; Yin, S; Qiu, R. Design and synthesis of C@$MoSe_2$@NMWCNT heterostructure as anode material for Na^+ Batteries via Mo-Based organic complexes. *Electrochimica Acta* **2023**, 461, 142598.

[24] Xu, J; Wu, D; Hao, J; Shen, J; Liu, Q; Zhang, P; Jiang, F. Advanced cathode materials for sodium-ion batteries. *Adv. Mater.* **2023**, 35, 2203087.